JGR Atmospheres

RESEARCH ARTICLE
10.1029/2018JD030222

Further Improvement of Surface Flux Estimation in the Unstable Surface Layer Based on Large-Eddy Simulation Data

S. Liu[1], X. Zeng[2], Y. Dai[1], and Y. Shao[3]

[1]Southern Marine Science and Engineering Guangdong Laboratory (Zhuhai), Guangdong Province Key Laboratory for Climate Change and Natural Disaster Studies, School of Atmospheric Sciences, Sun Yat-sen University, Guangzhou, China, [2]Department of Hydrology and Atmospheric Sciences, University of Arizona, Tucson, AZ, USA, [3]Institute of Geophysics and Meteorology, University of Cologne, Cologne, Germany

Key Points:
- Three-dimensional multiscale analysis technique is developed
- Multiscale turbulence processes are quantified in the unstable surface layer
- Practically applicable formula for the estimation of surface fluxes in the unstable surface layer is proposed

Supporting Information:
- Supporting Information S1
- Figure S1
- Figure S2
- Figure S3
- Figure S4
- Figure S5
- Figure S6
- Figure S7

Correspondence to:
S. Liu,
liushaof5@mail.sysu.edu.cn

Citation:
Liu, S., Zeng, X., Dai, Y., & Shao, Y. (2019). Further improvement of surface flux estimation in the unstable surface layer based on large-eddy simulation data. *Journal of Geophysical Research: Atmospheres*, *124*, 9839–9854. https://doi.org/10.1029/2018JD030222

Received 25 DEC 2018
Accepted 30 JUL 2019
Accepted article online 21 AUG 2019
Published online 4 SEP 2019

Abstract The Monin-Obukhov similarity theory (MOST) is widely used for the surface turbulence flux-gradient relations in modeling and data analysis. Here we quantify multiscale turbulence processes by applying our newly developed analysis technique to large-eddy simulation data, and find that in the unstable surface layer, large convective eddies (with the scaling of boundary layer depth) and local free convection exist in addition to small eddies. An empirical MOST function (considering the last two processes only) is found to underestimate the surface friction velocity and heat flux both by about 30%. Much better results can be obtained using a function that explicitly considers all three processes. Generally, the nondimensional wind shear exhibits larger scatter and deviates more from the MOST than the temperature gradient. Based on these results, we propose the revised Sorbjan (1986, https://doi.org/10.1007/BF00120989) function (with coefficients determined from this study) for wind shear and MOST function for temperature gradient, for estimating surface fluxes in the unstable surface layer. The three-dimensional multiscale analysis method we develop in this study is of general nature and can be of interest for problems of three-dimensional multiscale process description in other disciplines.

1. Introduction

Land surface interacts with the atmosphere through surface-air exchanges (i.e., fluxes) of energy, mass, and momentum. Land-atmosphere interaction is widely recognized as a crucial component of numerical weather and climate models. Predictions of these numerical models are sensitive to the surface fluxes. No matter how high the resolution of a numerical model is, the surface fluxes are always subgrid-scale processes that cannot be explicitly resolved and must be parameterized. At present, in almost all such numerical models, from local and mesoscale to global models, the surface flux parameterization is based on the Monin-Obukhov similarity theory (MOST; Monin & Obukhov, 1954).

Since its proposal, the MOST has been a fundamental theory for studying the atmospheric surface layer (ASL). The actual concept of ASL was first introduced as a constant flux layer (Monin & Obukhov, 1954) and it was defined as the bottom layer where momentum and heat fluxes are sufficiently constant with height that the surface fluxes can be taken equal to the local fluxes at given height. In practice, the surface layer is defined as the bottom part of the atmospheric boundary layer where the fluxes vary by less than 10% of their magnitude with height. According to the MOST, the statistical structure of the surface layer, under horizontally homogeneous and quasi-stationary conditions, is governed by only four independent parameters: height above ground, surface friction velocity, kinematic surface temperature flux, and a buoyancy parameter. An indispensable assumption implied in the MOST is that the surface layer is dominated by local shear-generated small eddies, while the influences of the large convective eddies or local buoyancy-driven motions are excluded.

The Monin-Obukhov similarity hypothesis has been widely tested with field measurements for mean wind and mean temperature gradients (e.g., Businger et al., 1971; Dyer, 1974; Hogstrom, 1988; Johansson et al., 2001; Salesky & Chamecki, 2012), for velocity and temperature variances (e.g., Banta, 1985; Johansson et al., 2001; Panofsky et al., 1977) or their spectra (e.g., Kaimal, 1978; Kaimal et al., 1972), and even tested with regard to the structure parameters (e.g., Li et al., 2012; Maronga, 2014). For the mean wind and

temperature gradients, the Monin-Obukhov similarity was reported to be verified by field experiments with the respective functional relationships determined (e.g., Businger et al., 1971; Dyer, 1974; Hogstrom, 1988). It is these universal functions (i.e., nondimensional gradients) that are used in numerical meteorological models to relate surface fluxes to relevant bulk meteorological quantities. The nondimensional gradients from individual experiments, however, exhibit a considerable degree of scatter (Hogstrom, 1996). Such scatter is often attributed to random errors. However, it was reported that random errors are not able to fully account for the scatter in the nondimensional gradients (Salesky & Chamecki, 2012). This finding suggests that in the surface layer there may exist physical processes that are neglected in the MOST and, as a result, the nondimensional gradients may also be a function of some parameters which describe these neglected processes but are not included in the aforementioned four parameters.

It has been shown via large-eddy simulation (LES; Khanna & Brasseur, 1997) and field experiments (Johansson et al., 2001) that under convective conditions, the nondimensional gradient of wind in the surface layer strongly depends on the boundary layer depth. The boundary layer depth is typically considered as the characteristic length scale of large convective eddies. The influence of such large eddies can be represented by explicitly including the boundary layer depth in the universal similarity functions (Sorbjan, 1986). While in many numerical weather and climate models, it is partially considered by including the convective velocity scale in calculating the nondimensional wind shear for the standard MOST (e.g., Zeng et al., 1998).

Through the analysis of the velocity variance (e.g., Panofsky et al., 1977) or further the velocity spectra (e.g., Kaimal, 1978; Kaimal et al., 1976; McNaughton et al., 2007; McNaughton & Laubach, 2000), it has been reported that in the unstable surface layer, horizontal and vertical velocity fluctuations scale differently. While vertical velocity fluctuations scale with the height above ground and therefore follow the Monin-Obukhov similarity, the horizontal velocity fluctuations scale with the boundary layer depth. In the boundary layer, three-dimensional turbulent eddies extend horizontally and vertically. The horizontal and vertical extent of turbulent eddies can be used to characterize turbulence horizontally and vertically, respectively (Liu et al., 2015). However, in most cases, it is in the vertical direction that the turbulent transport is of great interest, and therefore, the vertical extent is preferable to be used for turbulence scaling.

Recently, a new multiscale decomposition method, the orthogonal PDF decomposition (OPD) (Liu et al., 2015), has been proposed for pattern recognition and scale decomposition. It has been applied to surface heterogeneity quantification and turbulence structure identification (Liu et al., 2015, 2016). The OPD performs decomposition in the PDF domain and its reconstruction for nonperiodic signals can be done more effectively than that of traditional wave-based transforms (e.g., Fourier transform, wavelet transform) which are performed in the physical space. More importantly, many previous applications of the wave-based transforms to the atmospheric boundary layer turbulence are limited to the time domain or spatially the horizontal directions. In this study, we extend the OPD technique to three dimensions by allowing horizontal patches at neighboring heights to connect with each other to form three-dimensional patches. The vertical extents of these three-dimensional patches represent the vertical scales of turbulent eddies. By using this three-dimensional OPD technique, the multiscale processes in the unstable surface layer, with respect to vertical scaling, can be explicitly identified. Turbulence in the boundary layer, due to gravity and buoyancy, is apparently anisotropic. Without the three-dimensional OPD technique, the vertical turbulence scale would not be possible to be easily decomposed. Here we use this technique to address two questions: if large convective eddies do exist in the surface layer, how will they influence the flux-gradient relations there, or in response to them how will the flux-gradient relations depart from the standard Monin-Obukhov similarity? And what flux-gradient relations can be used to estimate surface fluxes for the unstable condition?

2. Theory and Methods

In this section, we will first present briefly the OPD technique and its extension to three dimensions (see Method S1 in the supporting information for details). The standard MOST and previous efforts to improve the flux-gradient relations for the unstable condition will be described as well. Finally, we will describe how the data used in this study are obtained via large-eddy simulation.

2.1. Orthogonal PDF Decomposition

Adopting the "mosaic of patches" idea in the area of large-scale atmospheric modeling, Liu et al. (2015) proposed the OPD technique for pattern recognition and scale decomposition. The OPD extends patches of land surface to patches of motions or other one- or two-dimensional physical quantities. The patches are recognized based on the reconstructed field which is obtained via an orthogonal transform in the PDF domain, in contrast to the traditional wave-based transforms (e.g., Fourier transform, wavelet transform) in the physical space.

For the horizontal reconstructed fields, a connected area with the same approximation is recognized as a patch. For each recognized patch, its horizontal extent is defined as its horizontal length scale (Liu et al., 2015). Therefore, the signal details are horizontal scale related and the energy spectrum can be expressed as a function of horizontal length scale. If horizontal patches at different heights connect with each other to form three-dimensional patches, then vertical draughts occur. For a three-dimensional patch, its vertical extent can be simply defined as its vertical length scale. Therefore, the signal details are vertical scale related and the energy spectrum can be expressed as a function of vertical length scale in the form of

$$E_{L_{\mathrm{vert}}} = \int_{-\infty}^{\infty} |D_{L_{\mathrm{vert}}}(s)|^2 \mathrm{d}s \tag{1}$$

where s represents space, L_{vert} denotes the vertical length scale, and $D_{L_{\mathrm{vert}}}(s)$ is the vertical-scale-dependent detail. The energy spectrum as a function of vertical length scale (equation (1)) is used in this study for identifying the multiscale processes in the unstable boundary layer. For more details, please refer to Method S1.

2.2. Monin-Obukhov Similarity Theory

The standard MOST assumes that under horizontally homogeneous and statistically stationary conditions the statistical structure of the ASL is governed by only four independent parameters: height z, surface friction velocity u_*, surface kinematic heat flux $\overline{(w'\theta')}_0$, and buoyancy parameter g/Θ_0. These governing parameters form a single nondimensional MOST stability parameter $\zeta = z/L$, where

$$L = -\frac{u_*^3 \Theta_0}{\kappa g \overline{(w'\theta')}_0} \tag{2}$$

is the Obukhov length. Here κ is the von Kármán constant, g is the acceleration of gravity, and the subscript 0 denotes the value at surface.

The MOST predicts that any mean flow or average turbulence quantity in the ASL, when normalized by an appropriate combination of the above-mentioned four independent parameters, should be a unique function of z/L. The nondimensional wind and temperature gradients are usually expressed as

$$\frac{\kappa z}{u_*}\frac{\partial U}{\partial z} = \phi_{\mathrm{m}}\left(\frac{z}{L}\right) \tag{3}$$

$$\frac{\kappa z}{\theta_*}\frac{\partial \Theta}{\partial z} = \phi_{\mathrm{h}}\left(\frac{z}{L}\right) \tag{4}$$

where U is the mean wind speed, Θ is the mean temperature, and $\theta_* = -\overline{(w'\theta')}_0/u_*$ is the temperature scale. Here $\phi_{\mathrm{m}}(z/L)$ and $\phi_{\mathrm{h}}(z/L)$ are the universal similarity functions which relate the constant fluxes

$$\tau = \tau_0 = \rho u_*^2 \tag{5}$$

$$H = H_0 = -\rho c_p u_* \theta_* \tag{6}$$

to the mean gradients in the surface layer, where τ represents the momentum flux, and H the heat flux.

2.3. Flux-Gradient Relations for Unstable Conditions

Since the proposal of the MOST, much field experimental effort has been spent on determining the universal functions $\phi_{\mathrm{m}}(z/L)$ and $\phi_{\mathrm{h}}(z/L)$ in equations (3) and (4). Based on previous individual experiments, Hogstrom (1996) suggested the universal functions for the unstable surface layer in the forms of

$$\phi_m\left(\frac{z}{L}\right) = \left(1-19\frac{z}{L}\right)^{-1/4} \tag{7}$$

$$\phi_h\left(\frac{z}{L}\right) = 0.95\left(1-11.6\frac{z}{L}\right)^{-1/2} \tag{8}$$

To account for the effects of large convective eddies, Zeng et al. (1998) proposed to add a convective velocity scale to the mean wind speed as

$$U = \left[U_x^2 + U_y^2 + (\beta w_*)^2\right]^{1/2} \tag{9}$$

for calculating the wind gradient in equation (3). In equation (9), U_x and U_y are the mean wind components, β is a weighting parameter (usually taken as unity), and w_* is the convective velocity scale:

$$w_* = \left(-\frac{g}{\Theta}u_*\theta_* z_i\right)^{1/3} \tag{10}$$

where z_i is the convective boundary layer depth.

Another strategy to account for the contribution of large convective eddies is to include the boundary layer depth z_i in the list of the governing parameters, which statistically characterize the ASL (e.g., Khanna & Brasseur, 1997; Sorbjan, 1986). More specifically, Sorbjan (1986) proposed the universal similarity functions in equations (3) and (4) in the forms of

$$\phi_m = C_m\left(-\frac{z}{L}\right)^{-1/3}\left(1-\alpha\frac{z}{z_i}\right)^{2/3} \tag{11}$$

$$\phi_h = C_h\left(-\frac{z}{L}\right)^{-1/3}\left(1-\alpha\frac{z}{z_i}\right)^{2/3} \tag{12}$$

where C_m, C_h, and α are the constants to be determined. According to Sorbjan (1986), α is the ratio of z_i to the height where the heat flux becomes zero. For C_m and C_h, there was no clear explanation and they are experiment dependent. Their determination is not trivial and should be carefully done.

3. Large-Eddy Simulation Data

It is assumed here that the structures of the surface layer can be mainly, if not completely, described via LES technique. LES is a numerical modeling approach that explicitly resolves large energy-containing turbulent eddies but parameterizes the less important small eddies. LES models have been under development since the 1960s (e.g., Deardorff, 1970, 1972; Mirocha et al., 2010; Moeng, 1984; Raasch & Harbusch, 2001; Smagorinsky, 1963; Sullivan et al., 1994). In this study, we use the LES of the Weather Research and Forecasting model (WRF; Skamarock et al., 2008) to generate data. The WRF-LES model has been widely used for the studies of atmospheric boundary layer turbulence (e.g., Catalano & Moeng, 2010; Liu et al., 2011; Moeng et al., 2007) and land-atmosphere interactions (e.g., Liu & Shao, 2013; Shao et al., 2013).

For the LES applications, all WRF physical options are turned off, except for the diffusion scheme. A subgrid-scale (SGS) model based on the 1.5-order turbulence kinetic energy diffusion scheme (Deardorff, 1980) is used to represent the subgrid-scale turbulence. With the WRF-LES model, four numerical experiments are carried out. For each experiment, the simulation time period is 2 hr, with a time step of 0.05 s. The simulation domain is 2 km × 2 km with a grid spacing of 5 m in the horizontal directions, and 600 m with a grid spacing of 2 m in the vertical. The top boundary is assumed to be at constant pressure with zero vertical velocity and free slip for each horizontal velocity. The lateral boundaries are periodic in each direction. The surface heat flux (0.06 K m s^{-1}) is specified, and the surface stresses are estimated at each grid point from

$$\tau_{xz}^{\text{surf}} = -C_D\left[\sqrt{(u_1)^2 + (v_1)^2}\right]u_1 \tag{13}$$

and

$$\tau_{yz}^{\text{surf}} = -C_D\left[\sqrt{(u_1)^2 + (v_1)^2}\right]v_1 \tag{14}$$

Here subscript 1 denotes the first model grid point above the surface for which the resolved-scale u and v are computed and C_D is the drag coefficient. The C_D is specified for each experiment (e.g., 0.008 for the baseline experiment W4 with background wind speed of 4 m/s) to generate different surface stress forcing. For all the simulations, initial conditions are horizontally homogeneous, with idealized atmospheric profiles. The initial potential temperature is constant with height (298 K) below 450 m. A capping inversion of 0.06 K/m is imposed between 450 and 550 m and constant temperature for above, with an initial boundary layer depth (z_i) set to 450 m. For simplicity, moisture is excluded. Zero mean wind is imposed in the y direction, but in the x direction varying background wind is set for different experiments (denoted as W4, W6, W8, and W10 for background wind speed of 4, 6, 8, and 10 m/s, respectively). The output frequency of data is once a minute. The first hour of simulation is regarded as spin-up time, and data of the second hour are used for the analysis in this study.

4. Results

The primary structures of a typical convective boundary layer are first discussed based on the baseline simulation W4. We then discuss how to apply the three-dimensional OPD to identify the relevant multiscale processes, especially those involved in the surface layer. The impact of these processes on the flux-gradient relations in the surface layer is demonstrated as well. Finally, flux-gradient relations for estimating surface fluxes in the unstable surface layer are examined.

4.1. Convective Boundary Layer Structures

Figure 1 shows hourly averaged vertical profiles of normalized fluxes of heat and momentum and those of potential temperature and wind speed. As can be seen, the potential temperature decreases and wind speed increases quickly with height near the surface, and then both remain almost constant until the capping inversion layer. The normalized heat flux profile is linear through the boundary layer and it has a minimum flux ratio (just below z_i) of about −0.16 (Figure 1a), which is close to the traditionally used value of −0.2 (Deardorff, 1979). The profile of momentum flux along the background wind is almost linear through the boundary layer as well, while that in the perpendicular direction is almost constantly zero (Figure 1b). These results suggest that a typical convective boundary layer is well simulated.

Turbulence in the shear-free convective boundary layer is well known to be principally characterized by Benard-type cells of narrow uprising plumes (updrafts) and wide downdrafts in between, wherein the updrafts likely connect with each other to form quasi-hexagonal shapes. On the other hand, the horizontal structures of a neutral boundary layer are generally characterized by large-scale organized motions (see Figure S1a). Therefore, the sheared convective boundary layer, which occurs more often in nature, should exhibit turbulent structures somehow between the above two extremes. Figure 2 shows that horizontally the turbulent vertical velocity displays narrow uprising areas with relatively wide downdrafts in between. Due to the wind shear, the uprising areas are more compact than those of the shear-free case and they are hardly able to connect with each other to form quasi-hexagonal shapes. These main features hold for both the two heights, except that higher level exhibits larger structures. These phenomena are more obvious in Figure S4 of the supporting information. Turbulence in the convective boundary layer, due to gravity and stratification, is three dimensional and anisotropic in the vertical direction. Therefore, as shown in Figure 2, vertical structures of the turbulent vertical velocity differ significantly from the horizontal structures. Horizontal patches of motions at different heights connect with each other to form three-dimensional motions (Figure 2).

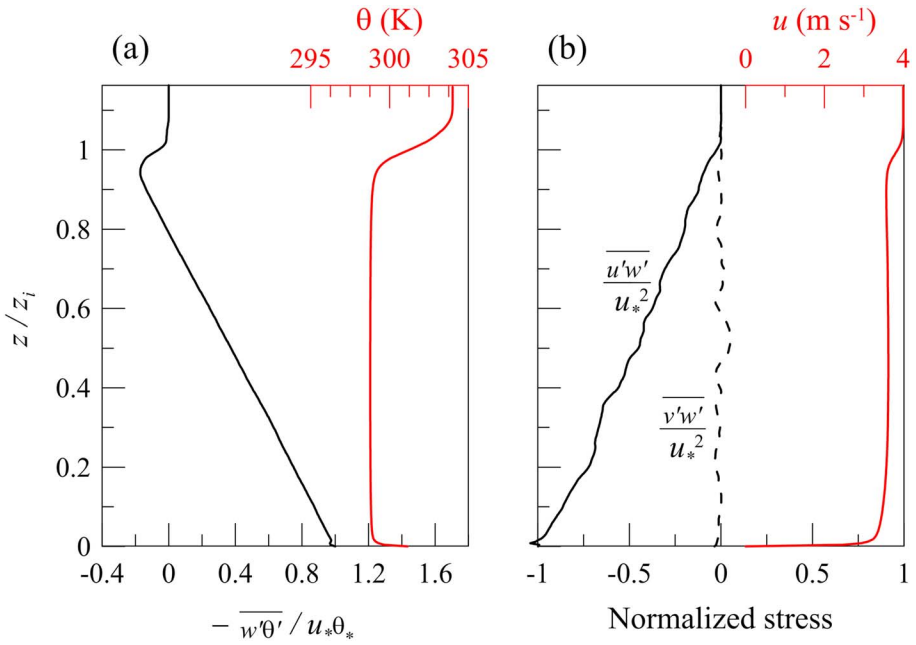

Figure 1. Vertical profiles of 1-hr and domain averaged (a) potential temperature (θ) and its normalized vertical flux ($\overline{w'\theta'}/u_*\theta_*$) and (b) normalized stress ($\overline{u'w'}/u_*^2$ and $\overline{v'w'}/u_*^2$ for u and v wind components, respectively) and u wind speed. Data here and below are, unless otherwise noted, from the baseline simulation.

We do not examine in detail the horizontal turbulence scales involved in the vertical turbulent transport; our interest is about the vertical turbulence scales. Therefore, the three-dimensional OPD presented in section 2.1 is applied to the sheared convective boundary layer to identify the multiscale turbulence processes with respect to vertical length scale.

4.2. Identification of Multiscale Processes

Vertical velocity variance can be taken as a measure of the strength of vertical motions, which are responsible for the vertical turbulent transport of scalars and momentum. Figure 3a shows that vertical velocity variance is small near the surface, but it increases quickly to a maximum at about one third of the boundary

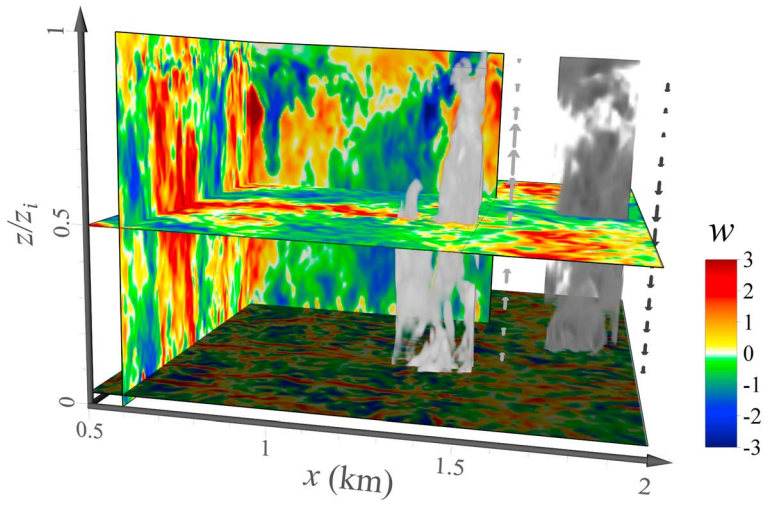

Figure 2. An instantaneous three-dimensional pattern of vertical velocity (with the horizontal mean removed and then normalized by the spatial standard deviation), with several cross sections shown in colors. Light and dark grey three-dimensional patches with corresponding arrows indicate updrafts and downdrafts, respectively, with longer arrows representing stronger movements and vice versa.

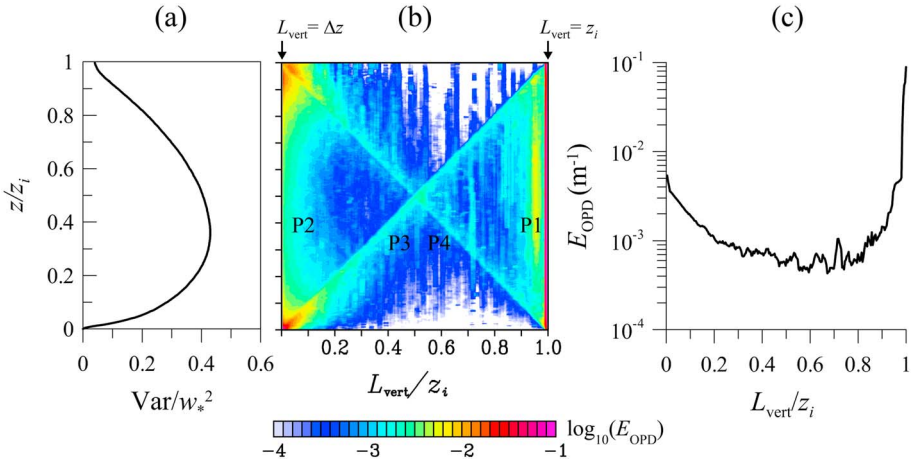

Figure 3. (a) Variance of the vertical velocity and (b) its OPD energy spectra as a function of vertical length scale L_{vert} at different heights, with four significant peaks, respectively, indicated by P1, P2, P3, and P4. (c) The variance-weighted mean OPD spectra for the whole boundary layer. Heights and vertical length scales are normalized by the boundary layer depth z_i, and variance is normalized by the convective velocity scale, w_*.

layer height, and then decreases with height. This variance profile is as expected (Stull, 1988). Note that the variance shown here is only the resolved part. For a typical large-eddy simulation, the subgrid energy is usually about 15% of the total energy in the flow interior (far from the boundaries), while as the surface is approached it becomes more significant (Mason & Thomson, 1992).

Applying the three-dimensional OPD, the vertical velocity variance (resolved-scale) is decomposed and presented as energy spectrum on the vertical length scales, with four distinct energy peaks (Figure 3b). The strongest one (P1) scales with z_i (L_{vert}~z_i) and remains almost through the whole boundary layer. The second peak (P2) is around the cutoff length scale (or the vertical grid spacing, Δz) of the LES grid mesh (L_{vert}~Δz), consistent with previous LES studies (e.g., Wyngaard et al., 1998). It strengthens significantly as the bottom or top boundary is approached. This peak represents the small eddy processes. The other two peaks (P3 and P4) lie along the two diagonals and, respectively, scale with the height above ground and the distance from the top of the boundary layer. They represent the local free convections originating from the surface and the convections originating locally but capped by the inversion layer, respectively. Eddies originating from the surface and extending to height z, indicated as peak P3, contribute to the energy at scale $L_{vert} = z$ for heights between the surface and z. For heights below z, there may be energy at scale $L_{vert} = z$ which is contributed by those eddies, but that energy is not a peak. Only at height z, the energy peaks at scale $L_{vert} = z$. In other words, eddies originating from the surface and extending to height z contribute relatively the most z-scale energy to height z.

On average, the OPD energy spectrum of the boundary layer exhibits a wide gap bounded by two distinct peaks (Figure 3c). This kind of spectral gap seems to be a desired representation of turbulence for the turbulence community (Farge et al., 1996; Liu et al., 2015). The dominant peak scales with the boundary layer depth, and the other one, significant but weaker by more than an order of magnitude, is around the cutoff length scale (Figure 3c). The energy decreases from the dominant peak to smaller scales until around the scale of half of the boundary layer depth. This can be understood as a traditional successive turbulent energy cascade process. This cascade process does not continue to the smallest scales, but instead is interrupted by an energy peak at the smallest scales. Close to the boundaries, the small eddies due to shear production are strengthened and energy is more concentrated in the subgrid scales, and the backscatter, that is, local transfer of energy from subgrid to resolved scales, becomes more significant (Mason & Thomson, 1992). Logically this kind of backscatter should continue to resolved scales to transfer energy from small to larger resolved scales. It is well known that the shear production generates the energy in the horizontal velocity components, from which the energy can be partly taken into the vertical component via the pressure redistribution. In our case, the wind shear contributes little (compared to the buoyancy) to the vertical velocity variance (not shown here). Thus, the backscatter process arising from the wind shear should also contribute little

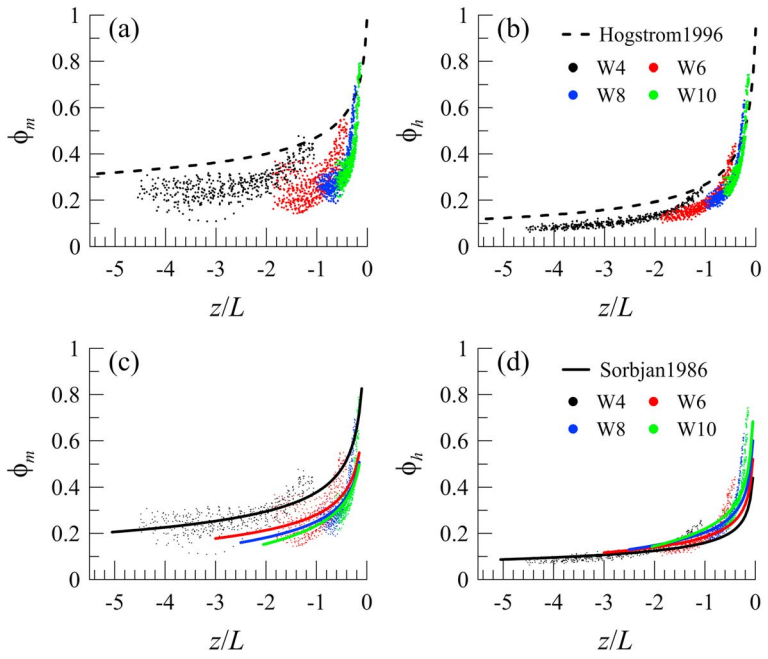

Figure 4. MO-normalized (a and c) mean wind shear and (b and d) mean temperature gradient against z/L of the four LES experiments with four different initial background wind speeds. The dashed lines are the empirical curves suggested by Hogstrom (1996) according to multiple individual field measurements. The solid lines (in four corresponding colors) are the empirical curves proposed by Sorbjan (1986).

to the energy spectrum as shown in Figure 3c. Rather, the energy spectrum is mainly determined by the buoyancy. Another important issue is how the energy cascade process of the large convective eddies is driven by the buoyancy and how the energy is transferred between scales with respect to vertical scaling. We will discuss this issue in detail in a separate paper.

Figure 3b shows that near the surface large convective eddies and local free convection appear to coexist with small eddy processes. This can be revealed even more clearly by the OPD energy spectral curves for two specific heights near the surface (see Figure S5. For more details, please refer to Text S1 in the supporting information. Then, a further question is how the former two types of processes affect the flux-gradient relations in the surface layer.

4.3. Impact on the Flux-Gradient Relations

The two empirical universal similarity functions suggested by Hogstrom (1996) as shown in equations (7) and (8) are used as a reference to test the flux-gradient relations in the unstable surface layer based on the LES data.

As mentioned in the first section, the surface layer in practice is defined as the bottom part of the boundary layer where the fluxes vary by less than 10% of their magnitude with height. For the LES, as the surface is approached fluxes increasingly occur on the subgrid scale and the SGS parameterization plays an increasingly important role. To eliminate as much as possible the influence of the SGS scheme, only the LES data of the heights which are within the surface layer and where more than 90% of the total flux is explicitly resolved are used for analysis. For each time step and each height of interest, each of the four LES experiments has a nondimensional wind gradient, calculated according to equation (3), and a nondimensional temperature gradient, calculated according to equation (4). All these gradients are then plotted against z/L in comparison with the corresponding empirical curves as shown in Figure 4.

The simulated dimensionless wind gradient ϕ_m generally shows the similar tendency as the empirical curve (Figure 4a). Quantitatively, however, they show significant departures from the empirical curve. Moreover, the ϕ_m data of the four simulations do not collapse to a single curve and have a high degree of scatter. Within a simulation, they all show steeper gradients than the empirical relation, in agreement with results of

Table 1
Parameters Related to Equations (11) and (12) Set for Different Experiments

Experiment	α	$-z_i/L$	C_m	C_h
W4	1.28	53.1	0.384	0.162
W6	1.31	21.4	0.293	0.192
W8	1.39	11.9	0.273	0.222
W10	1.5	7.7	0.27	0.253
Sobjan1986	1.5	100	0.6	0.25

previous numerical studies (Li et al., 2018; Pirozzoli et al., 2017). Notice that for a specific simulation the variable z/L is obtained by varying z with nearly fixed L. The scatter in ϕ_m is seen to increase with negative z/L, thus actually increases with height. This kind of increase of scatter, we argue, is attributed to the increasing large-eddy effects with height in the region near the surface (see Figure S5). Although there is considerable scatter among the data in each stability (measured by z_i/L) group of simulation, there is a significant and clear ordering of the four data sets, with the most unstable data group on the left and the least on the right in Figure 4a. More importantly, each group has distinct collapse pattern and as a whole they fail to form a single curve as MO predicted. The MO parameters may be appropriate normalizing scales since the ϕ_m is on the order of 1 for all four simulations, but a systematic dependence on z_i should exist to take into account the effects of z_i-scale large-eddy processes (Khanna & Brasseur, 1997; Li et al., 2018), which together with the local free convection have been identified clearly in the last section. The local free convection scales on z, therefore, it is not necessary to introduce new scaling parameter to account for its effect.

The dimensionless temperature gradient ϕ_h data appear to collapse much better onto a single curve and exhibit much less scatter than the corresponding ϕ_m (Figure 4b), in agreement with previous numerical studies (Khanna & Brasseur, 1997; Li et al., 2018; Pirozzoli et al., 2017) and field measurements (Johansson et al., 2001; Salesky & Chamecki, 2012). The reason is that the wind shear in the surface layer is affected more than the temperature gradient by the large-eddy processes. Vertical fluxes in the boundary layer are mainly transported by turbulent eddies of different scales. Thus, the flux spectra of momentum or heat in the surface layer are similar to the energy spectrum (see Figure S6a). The z_i-scale large eddies can transport momentum and heat or other scalars efficiently between the surface layer and the top of the boundary layer. However, due to the existence of the capping inversion layer and the large geostrophic wind speed near there, the mean temperature difference between the surface layer and the top of the boundary layer is relatively smaller than that of mean wind speed (Figure 1). Therefore, in comparison with the heat flux, the momentum flux is contributed more by the z_i-scale large eddies (see Figure S6b). Thus, the z_i-scale large eddies lead to relatively stronger effects on the velocity field than on the temperature field in the surface layer.

The above analysis shows that the standard MOST cannot describe well the simulated flux-gradient relations in the unstable surface layer; for the scaling of those flux-gradient relations, the large-eddy processes should be considered. Based on the local free convection similarity hypothesis, Sorbjan (1986) theoretically proposed new forms of ϕ_m and ϕ_h for the unstable surface layer, which explicitly take into account the scale of z_i as described by equations (11) and (12). The three unknown parameters C_m, C_h, and α are to be determined. According to Sorbjan (1986), α is the ratio of z_i to the height where the heat flux becomes zero. There was no clear explanation for C_m and C_h, but evidently, they are experiment dependent.

The determination of α is straightforward; it is derived from the heat flux profiles in the boundary layer for different experiments. The coefficients C_m and C_h in equations (11) and (12) for each experiment are obtained based on a least-absolute-deviation regression using the LES data as shown in Figure 4. Values of the three parameters for different experiments are as shown in Table 1. To make the estimation of C_m and C_h practically predictable, there are two assumptions to be made beforehand. First, it is assumed that the simulated flux-gradient relations in the ASL are correct. It is justified since for the analysis region more than 90% of flux is explicitly resolved by the LES. Second, no new parameters are introduced in addition to the existing ones in equation (11) and (12) and C_m and C_h are a function of single parameter. From the mathematical perspective, C_m and C_h could be a function of α or z_i/L. As demonstrated in last section, there are three distinct types of processes in the ASL, that is, small eddies, local free convections, and z_i-scale large eddies. According to the existing theories, the function of z/L represents the effects of small eddies. z/z_i measures the relative position in the boundary layer and can be used to describe the effects of local free convections. The relative strength of z_i-scale large eddies is nearly independent of z (see Figure 4b). Logically, the z-independent parameter z_i/L should be used to represent the effects of z_i-scale large eddies. Furthermore, it was revealed that the wind shear in the unstable surface layer is affected more than the temperature gradient by the large-eddy processes and the dimensionless temperature gradient ϕ_h data

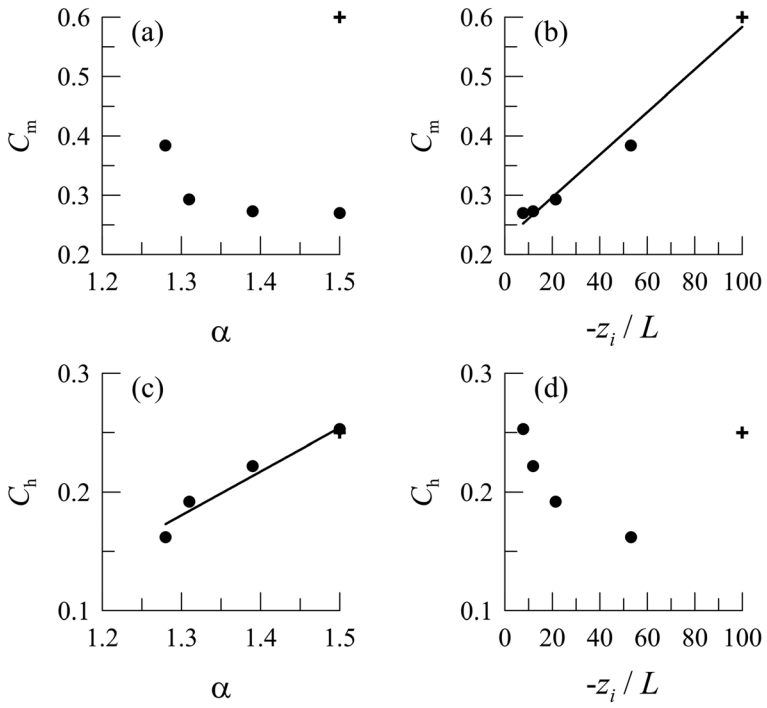

Figure 5. (a and b) C_m as a function of α and $-z_i/L$, respectively, using the data listed in Table 1. (c and d) Same as in (a) and (b) but for C_h. Dots represent data for LES experiments, and crosses data from Sorbjan (1986). The straight lines are the linear regression with a coefficient of determination (b) $R^2 = 0.98$ and (c) $R^2 = 0.96$ and confidence level greater than 99% for both.

appear to collapse much better onto a single curve (Figure 4b). From the physical perspective, therefore, C_m seems more likely to be a function of z_i/L and C_h of α.

If C_m is a function of α, that function should be universal. With the relevant parameters from Sorbjan (1986) included (Table 1), however, it is hard to see a consistent relationship between C_m and α anymore (Figure 5a). On the contrary, C_m holds a significant linear relationship with $-z_i/L$ (Figure 5b). The linear regression equation is

$$C_m = 0.0036\left(-\frac{z_i}{L}\right) + 0.2246 \tag{15}$$

for which the coefficient of determination R^2 is as high as 0.98 with confidence level greater than 99%. As for C_h, on the other hand, it is hard to see a consistent relationship between C_h and $-z_i/L$ (Figure 5d) and C_h holds a significant linear relationship with α (Figure 5c). The linear regression equation is

$$C_h = 0.3687\alpha - 0.2989 \tag{16}$$

with the coefficient of determination R^2 0.96 and confidence level greater than 99%.

By using the values of α, C_m, and C_h as listed in Table 1, we can plot equations (11) and (12) in comparison with the LES results as shown in Figure 4. The wind shear relation of Sorbjan (1986) is obviously more consistent with the simulation data than the standard MOST empirical one (Figure 4c). The simulated temperature gradient, in contrast, does not necessarily agree better with the Sorbjan (1986) curves (Figure 4d). Rather, it generally follows the standard MOST (Figure 4b).

4.4. Estimation of Surface Fluxes in the Unstable Surface Layer

In this section, the empirical functions described in section 2.3 for the unstable surface layer are examined in terms of the biases of their estimated surface fluxes. The examination is carried out for the four experiments. According to equation (3), we have

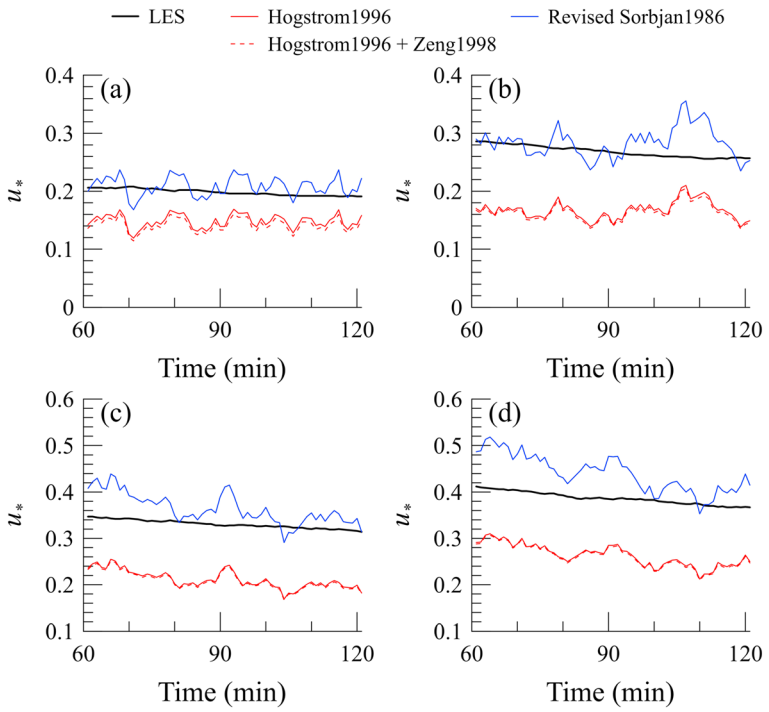

Figure 6. Surface friction velocity simulated by LES and that estimated according to different empirical schemes for experiments (a) W4, (b) W6, (c) W8, and (d) W10.

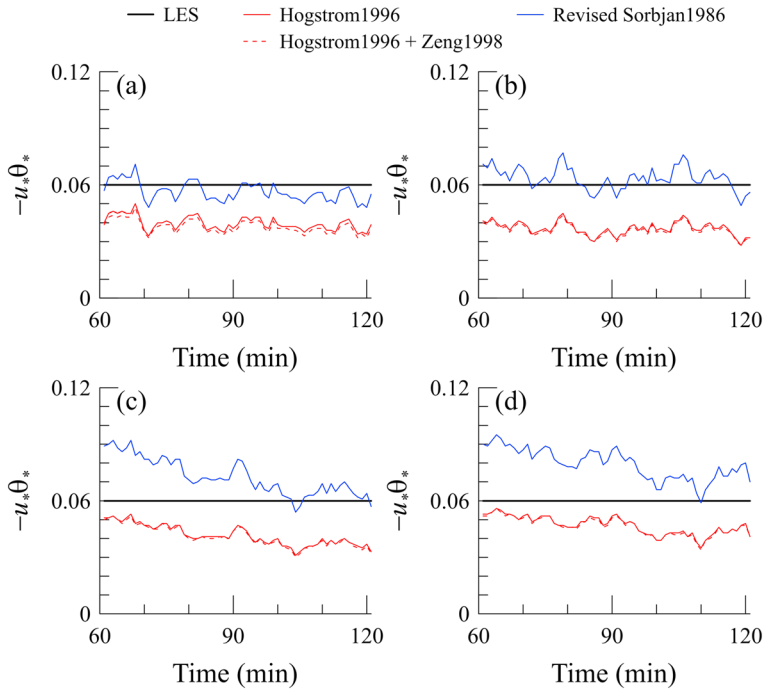

Figure 7. Same as Figure 6 but for surface heat flux.

Table 2
Statistics of the Estimated Surface Fluxes Via Different Empirical Flux-Gradient Relations and Their Comparison With LES

Experiment	Surface flux		Hogstrom (1996)	Hogstrom (1996) and Zeng et al. (1998)	Revised Sorbjan (1986)	LES
W4	u_*	Value	0.148	0.142	0.209	0.198
		Bias	−25%	−28%	6%	
	$-u_*\theta_*$	Value	0.040	0.038	0.056	0.060
		Bias	−33%	−37%	−7%	
W6	u_*	Value	0.167	0.163	0.284	0.269
		Bias	−38%	−39%	6%	
	$-u_*\theta_*$	Value	0.037	0.036	0.064	0.060
		Bias	−38%	−40%	7%	
W8	u_*	Value	0.221	0.208	0.364	0.331
		Bias	−33%	−37%	10%	
	$-u_*\theta_*$	Value	0.042	0.041	0.073	0.060
		Bias	−30%	−32%	22%	
W10	u_*	Value	0.263	0.261	0.440	0.387
		Bias	−32%	−33%	14%	
	$-u_*\theta_*$	Value	0.047	0.047	0.079	0.060
		Bias	−22%	−22%	32%	

$$u_* = \frac{\kappa z}{\phi_m}\frac{\partial U}{\partial z} \tag{17}$$

The data of the heights at which the nondimensional gradient calculation is done in section 4.3 are used here for calculating the surface friction velocity u_*. That is to say, the calculation is done for the heights which are within the surface layer and where more than 90% of the total flux is explicitly resolved. U is the horizontally averaged wind speed. ϕ_m is set according to the empirical functions to be examined. For each experiment and each time step, each height of interest gets au_*, which is calculated from equation (17). The u_* averaged over heights is taken as the estimated u_* for the surface layer. The evolution of the estimated u_* with time for each experiment is as shown in Figure 6, in which the u_* specified in LES is used as the reference for comparison. As shown in Figure 6 the empirical MOST function (Hogstrom, 1996) underestimates the u_*. This cannot be improved by including the convective velocity scale in calculating the mean shear with the parameter $\beta = 1$ in equation (9) (Zeng et al., 1998). The wind shear in Zeng et al. (1998) is integral and $\beta = 1$ can account for partly the effects of large eddies on the whole surface layer. But for the wind shear at specific level $\beta = 1$ cannot. The revised Sorbjan (1986) function (with coefficients determined by equation (15)) increases greatly the estimation. The estimation for the modest background wind speed conditions (W4 and W6) agrees quite well with the reference (Figures 6a and 6b). But for the high background wind speed

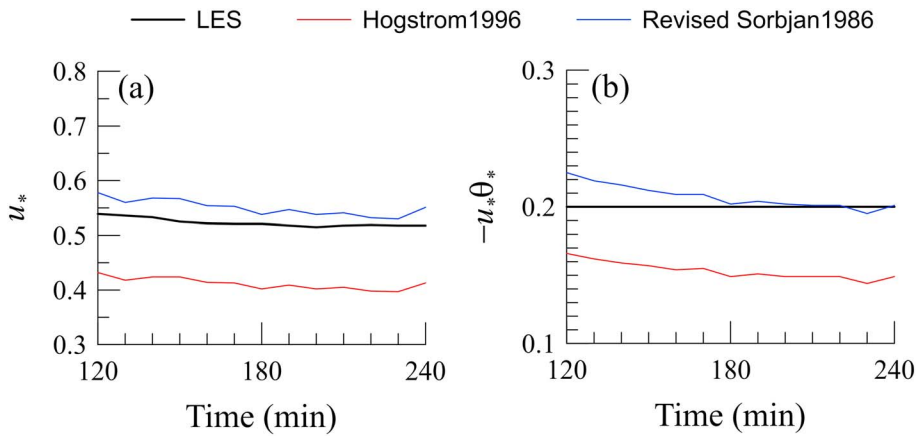

Figure 8. (a) Surface friction velocity and (b) surface heat flux simulated by LES (Zhou et al., 2018, 2019) and those estimated according to different empirical schemes.

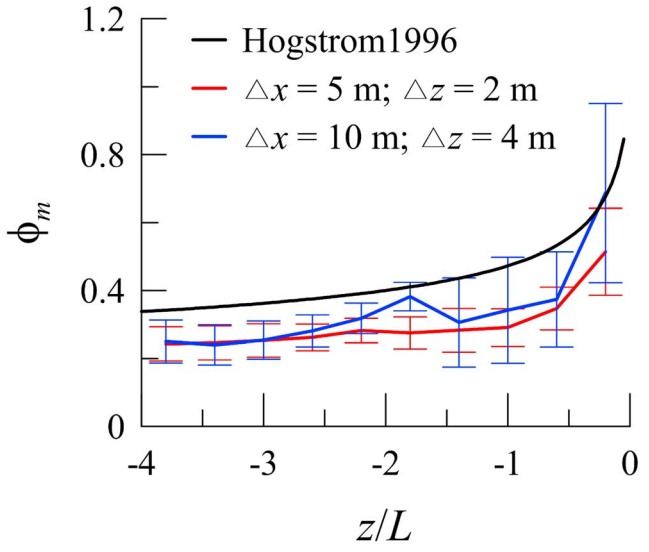

Figure 9. MO-normalized mean wind shear against z/L for the default set of LES experiments and another set of simulations with a twice coarser spatial resolution. Data are sample averaged, with the standard deviations indicated by vertical bars. The dark curve is from Hogstrom (1996).

conditions (W8 and W10), the overestimation is visible (Figures 6c and 6d). The estimated u_* all oscillate with a period of around 10 min, the typical oscillation period of large eddies, reflecting the large-eddy effect in the unstable surface layer.

Similarly, according to equation (4), we have

$$\theta_* = \frac{\kappa z}{\phi_h}\frac{\partial \Theta}{\partial z} \tag{18}$$

We set the ϕ_h according to the empirical MOST function, since as shown by the LES data it generally follows the MOST (Figure 4b). For each experiment and each time step, according to equation (18) each height of interest gets an estimated θ_*. The product $-u_*\theta_*$, which is exactly the surface heat flux, is then averaged over heights and the temporal evolution of the estimated $-u_*\theta_*$ is obtained as shown in Figure 7, in which the heat flux specified in LES is used as the reference for comparison. Generally, the estimated $-u_*\theta_*$ behaves quite similar to the u_*. This is understandable since the θ_* is estimated from the same empirical function; thus, it is the u_* that makes the difference for the $-u_*\theta_*$. Similarly, the empirical MOST function underestimates the $-u_*\theta_*$. This also cannot be improved by including the convective velocity scale in calculating the mean shear. By increasing the estimation of u_*, the revised Sorbjan (1986) function increases greatly the estimation of $-u_*\theta_*$. The estimation for the modest background wind speed conditions (W4 and W6) agrees quite well with the reference (Figures 7a and 7b). But for the high background wind speed conditions (W8 and W10), the overestimation of $-u_*\theta_*$ is even larger than that for u_* (Figures 6c and 6d). This obviously is due to the nonnegligible biases in the estimation of θ_*.

As shown in Table 2, the empirical MOST function underestimates the u_* and $-u_*\theta_*$ by around 30%. Including the convective velocity scale in calculating the mean shear with $\beta = 1$ in equation (9) makes no difference to the estimation of surface fluxes. For the u_*, the revised Sorbjan (1986) function with parameters determined by equation (15) does the best estimation, with biases of only 6% for the modest and about 10% for the high background wind speed conditions. Accordingly, the estimation of $-u_*\theta_*$, for which the θ_* is estimated from the MOST function, is improved significantly with biases reduced to no more than 10% for the modest background wind speed conditions. For the high wind speed (10 m/s), however, the revised Sorbjan (1986) function does not perform that well for the estimation of $-u_*\theta_*$.

5. Conclusions and Discussion

The OPD (Liu et al., 2015) is extended to three dimensions. By applying the three-dimensional OPD, we have identified multiscale turbulence processes, with respect to vertical length scale, for an unstable boundary layer simulated by LES. More specifically, in the unstable surface layer, significant large (z_i-scale) convective eddy processes and local free convection have been revealed in addition to small eddy processes. The impact of the first two types of processes on the surface layer has been examined from the perspective of flux-gradient relations. It is shown that the large-eddy effect is an important factor for the simulated flux-gradient relations to deviate from the standard MOST. Generally, the nondimensional wind shear in the surface layer exhibits larger scatter and deviates more from the MOST than the temperature gradient. Moreover, the nondimensional wind shear shows significant dependence on the scale of z_i in addition to the dimensionless MOST stability parameter z/L. As for the nondimensional temperature gradient, the LES data have less scatter and generally follow the MOST, in consistence with previous studies.

The simulated nondimensional wind shear can be represented well by the revised Sorbjan (1986) empirical function, which depends explicitly on z_i. In contrast, the empirical MOST function (Hogstrom, 1996) underestimates the surface friction velocity u_* and heat flux $-u_*\theta_*$ both by around 30%. This kind of underestimation is not reduced by including the convective velocity scale in calculating the mean shear

with a constant β in equation (9). For the u_*, the revised Sorbjan (1986) function with parameters determined by equation (15) best estimates, with biases of only 6% for the modest and around 10% for the high background wind speed conditions. Accordingly, the estimation of $-u_*\theta_*$ is improved significantly with biases reduced to no more than 10% for the modest background wind speed conditions. Therefore, for the estimation of surface fluxes in the unstable surface layer, we propose the combined use of Sorbjan (1986) and MOST functions, that is, the revised Sorbjan (1986) function for wind shear (i.e., equation (11), with parameters determined by equation (15)) and MOST function for temperature gradient (i.e., equation (8)). The parameter α in equation (11) is the ratio of z_i to the height where the heat flux becomes zero. For the parameter C_m, equation (15) can be used for the specific range of $-z_i/L$ discussed in this study. More work with field measurements and numerical simulations needs to be done to improve this formula for the full range of $-z_i/L$.

We are aware that our LES simulation only covers a small set of flow conditions. To test the robustness of our results, we have applied our formula to the independent LES data generated by a different model with totally different flow and heat flux conditions (Zhou et al., 2018, 2019). We choose the case with high background wind speed (10 m/s) and high surface heating (prescribed constant surface heat flux of 0.20 K m^{-1} s^{-1}), in which neither wind shear nor buoyancy is too dominant. The data output frequency is once per 10 min. The simulation data of the second 2 hr are used for analysis (the averaged vertical profiles are shown in Figure S7). Compared to the similarity theory, our formula (without any changes) can significantly improve the estimated surface fluxes (Figure 8).

The data used in this study are obtained by the LES technique. In the flow interior of a typical LES, the total energy and flux are mainly resolved. But as the surface is approached, energy and flux increasingly occur on the subgrid scale. To eliminate as much as possible the influence of the SGS scheme, the data of the bottom layer where more than 10% of the total flux is estimated by the SGS scheme are discarded from the surface layer similarity analysis in this study. However, the uncertainty due to the SGS scheme certainly contributes to the bias in the derived flux-gradient relations. To reduce this kind of bias, we have two options. One is to apply more advanced SGS schemes which, for example, can reasonably consider the backscatter effects. The other is to increase the resolution, especially for the region near surface. Increasing resolution can resolve more energy explicitly and thus reduce the influence of the SGS uncertainty. To test this, we have another set of simulations with coarser spatial resolution. It is shown in Figure 9 that the higher resolution does not necessarily improve the sample averaged nondimensional wind shear, but it obviously reduces the uncertainty due to the SGS. Furthermore, Reynolds number effect could also potentially contribute to the uncertainty. To take into account this effect, sophisticated wall models (e.g., Li et al., 2016; Marusic et al., 2010), in which the "law of the wall" is based on the concept of universal behavior of momentum and scalars in the inertial (logarithmic) layer, can be applied to the LES.

Acknowledgments
This work was supported by the National Key R&D Program of China (under grant 2017YFA0604300), the Natural Science Foundation of China (under grants 41875128 and 41730962), and the German DFG Transregional Cooperative Research Centre 32 "Patterns in Soil-Vegetation-Atmosphere-Systems: Monitoring, Modelling and Data Assimilation." The Editor (Minghua Zhang) and the anonymous reviewer are thanked for constructive comments. Bowen Zhou is thanked for providing the new independent LES data set. The data for this paper will be archived and available at the database: https://pan.baidu.com/s/1ssux3IhtoJZMoAS1v7tb6w.

References

Banta, R. M. (1985). Late-morning jump in TKE in the mixed layer over a mountain basin. *Journal of the Atmospheric Sciences*, *42*(4), 407–411. https://doi.org/10.1175/1520-0469(1985)042<0407:LMJITI>2.0.CO;2

Businger, J. A., Wyngaard, J. C., Izumi, Y., & Bradley, E. F. (1971). Flux-profile relationships in the atmospheric surface layer. *Journal of the Atmospheric Sciences*, *28*(2), 181–189. https://doi.org/10.1175/1520-0469(1971)028<0181:FPRITA>2.0.CO;2

Catalano, F., & Moeng, C.-H. (2010). Large-eddy simulation of the daytime boundary layer in an idealized valley using the weather research and forecasting numerical model. *Boundary-Layer Meteorology*, *137*(1), 49–75. https://doi.org/10.1007/s10546-011-9518-8

Deardorff, J. W. (1970). A numerical study of three-dimensional turbulent channel flow at large Reynolds numbers. *Journal of Fluid Mechanics*, *41*(2), 453–480. https://doi.org/10.1017/S0022112070000691

Deardorff, J. W. (1972). Numerical investigation of neutral and unstable planetary boundary layers. *Journal of the Atmospheric Sciences*, *29*(1), 91–115. https://doi.org/10.1175/1520-0469(1972)029<0091:NIONAU>2.0.CO;2

Deardorff, J. W. (1979). Prediction of convective mixed-layer entrainment for realistic capping inversion structure. *Journal of the Atmospheric Sciences*, *36*(3), 424–436. https://doi.org/10.1175/1520-0469(1979)036<0424:POCMLE>2.0.CO;2

Deardorff, J. W. (1980). Stratocumulus-capped mixed layer derived from a three-dimensional model. *Boundary-Layer Meteorology*, *18*(4), 495–527. https://doi.org/10.1007/BF00119502

Dyer, A. J. (1974). A review of flux-profile relationships. *Boundary-Layer Meteorology*, *7*(3), 363–372. https://doi.org/10.1007/BF00240838

Farge, M., Kevlahan, N., Perrier, V., & Goirand, E. (1996). Wavelets and turbulence. *Proceedings of the IEEE*, *84*(4), 639–669.

Hogstrom, U. (1988). Non-dimensional wind and temperature profiles in the atmospheric surface layer: A re-evaluation. *Boundary-Layer Meteorology*, *42*(1-2), 55–78. https://doi.org/10.1007/BF00119875

Hogstrom, U. (1996). Review of some basic characteristics of the atmospheric surface layer. *Boundary-Layer Meteorology*, *78*(3-4), 215–246. https://doi.org/10.1007/BF00120937

Johansson, C., Smedman, A.-S., Hogstrom, U., Brasseur, J. G., & Khanna, S. (2001). Critical test of the validity of Monin-Obukhov similarity during convective conditions. *Journal of the Atmospheric Sciences*, *58*(12), 1549–1566. https://doi.org/10.1175/1520-0469(2001)058<1549:CTOTVO>2.0.CO;2

Kaimal, J. C. (1978). Horizontal velocity spectra in an unstable surface layer. *Journal of the Atmospheric Sciences*, *35*(1), 18–24. https://doi.org/10.1175/1520-0469(1978)035<0018:HVSIAU>2.0.CO;2

Kaimal, J. C., Wyngaard, J. C., Haugen, D. A., Cote, O. R., Izumi, Y., Caughey, S. J., & Readings, C. J. (1976). Turbulence structure in the convective boundary layer. *Journal of the Atmospheric Sciences*, *33*(11), 2152–2169. https://doi.org/10.1175/1520-0469(1976)033<2152:TSITCB>2.0.CO;2

Kaimal, J. C., Wyngaard, J. C., Izumi, Y., & Cote, O. R. (1972). Spectral characteristics of surface-layer turbulence. *Quarterly Journal of the Royal Meteorological Society*, *98*(417), 563–589. https://doi.org/10.1002/qj.49709841707

Khanna, S., & Brasseur, J. G. (1997). Analysis of Monin-Obukhov similarity from large-eddy simulation. *Journal of Fluid Mechanics*, *345*, 251–286. https://doi.org/10.1017/S0022112097006277

Li, D., Bou-Zeid, E., & De Bruin, H. A. R. (2012). Monin-Obukhov similarity functions for the structure parameters of temperature and humidity. *Boundary-Layer Meteorology*, *145*(1), 45–67. https://doi.org/10.1007/s10546-011-9660-y

Li, Q., Bou-Zeid, E., Anderson, W., Grimmond, S., & Hultmark, M. (2016). Quality and reliability of LES of convective scalar transfer at high Reynolds numbers. *International Journal of Heat and Mass Transfer*, *102*, 959–970. https://doi.org/10.1016/j.ijheatmasstransfer.2016.06.093

Li, Q., Gentine, P., Mellado, J. P., & McColl, K. A. (2018). Implications of nonlocal transport and conditionally averaged statistics on Monin–Obukhov similarity theory and Townsend's attached eddy hypothesis. *Journal of the Atmospheric Sciences*, *75*(10), 3403–3431. https://doi.org/10.1175/JAS-D-17-0301.1

Liu, G., Sun, J., & Yin, L. (2011). Turbulence characteristics of the shear-free convective boundary driven by heterogeneous surface heating. *Boundary-Layer Meteorology*, *140*(1), 57–71. https://doi.org/10.1007/s10546-011-9591-7

Liu, S., Hintz, M., & Li, X. (2016). Evaluation of atmosphere-land interactions in an LES from the perspective of heterogeneity propagation. *Advances in Atmospheric Sciences*, *33*(5), 571–578. https://doi.org/10.1007/s00376-015-5212-6

Liu, S., & Shao, Y. (2013). Soil layer configuration requirement for large-eddy atmosphere and land surface coupled modeling. *Atmospheric Science Letters*, *14*(2), 112–117. https://doi.org/10.1002/asl.426

Liu, S., Shao, Y., Hintz, M., & Lennartz-Sassinek, S. (2015). Multi-scale decomposition for heterogeneous land-atmosphere systems. *Journal of Geophysical Research: Atmospheres*, *120*, 917–930. https://doi.org/10.1002/2014JD022258

Maronga, B. (2014). Monin-Obukhov similarity functions for the structure parameters of temperature and humidity in the unstable surface layer: Results from high-resolution large-eddy simulations. *Journal of the Atmospheric Sciences*, *71*(2), 716–733. https://doi.org/10.1175/JAS-D-13-0135.1

Marusic, I., Mathis, R., & Hutchins, N. (2010). Predictive model for wall-bounded turbulent flow. *Science*, *329*(5988), 193–196. https://doi.org/10.1126/science.1188765

Mason, P. J., & Thomson, D. J. (1992). Stochastic backscatter in large-eddy simulations of boundary layers. *Journal of Fluid Mechanics*, *242*, 51–78. https://doi.org/10.1017/S0022112092002271

McNaughton, K. G., Clement, R. J., & Moncrieff, J. B. (2007). Scaling properties of velocity and temperature spectra above the surface friction layer in a convective atmospheric boundary layer. *Nonlinear Processes in Geophysics*, *14*(3), 257–271. https://doi.org/10.5194/npg-14-257-2007

McNaughton, K. G., & Laubach, J. (2000). Power spectra and cospectra for wind and scalars in a disturbed surface layer at the base of an advective inversion. *Boundary-Layer Meteorology*, *96*, 143–185.

Mirocha, J. D., Lundquist, J. K., & Kosovic, B. (2010). Implementation of a nonlinear subfilter turbulence stress model for large-eddy simulation in the Advanced Research WRF Model. *Monthly Weather Review*, *138*, 4212–4228.

Moeng, C.-H. (1984). A large-eddy simulation model for the study of planetary boundary-layer turbulence. *Journal of the Atmospheric Sciences*, *41*(13), 2052–2062. https://doi.org/10.1175/1520-0469(1984)041<2052:ALESMF>2.0.CO;2

Moeng, C.-H., Dudhia, J., Klemp, J., & Sullivan, P. (2007). Examining two-way grid nesting for large eddy simulation of the PBL using the WRF model. *Monthly Weather Review*, *135*(6), 2295–2311. https://doi.org/10.1175/MWR3406.1

Monin, A. S., & Obukhov, A. M. (1954). Basic laws of turbulent mixing in the atmospheric surface layer. *Contributions of the Geophysical Institute, Slovak Academy of Sciences*, *24*, 163–187.

Panofsky, H. A., Tennekes, H., Lenschow, D. H., & Wyngaaard, J. C. (1977). The characteristics of turbulent velocity components in the surface layer under convective conditions. *Boundary-Layer Meteorology*, *11*(3), 355–361. https://doi.org/10.1007/BF02186086

Pirozzoli, S., Bernardini, M., Verzicco, R., & Orlandi, P. (2017). Mixed convection in turbulent channels with unstable stratification. *Journal of Fluid Mechanics*, *821*, 482–516. https://doi.org/10.1017/jfm.2017.216

Raasch, S., & Harbusch, G. (2001). An analysis of secondary circulations and their effects caused by small-scale surface inhomogeneities using large-eddy simulation. *Boundary-Layer Meteorology*, *101*(1), 31–59. https://doi.org/10.1023/A:1019297504109

Salesky, S. T., & Chamecki, M. (2012). Random errors in turbulence measurements in the atmospheric surface layer: Implications for Monin-Obukhov similarity theory. *Journal of the Atmospheric Sciences*, *69*(12), 3700–3714. https://doi.org/10.1175/JAS-D-12-096.1

Shao, Y., Liu, S., Schween, J., & Crewell, S. (2013). Large-eddy atmosphere-land surface modeling over heterogeneous surfaces: Model development and comparison with measurements. *Boundary-Layer Meteorology*, *148*(2), 333–356. https://doi.org/10.1007/s10546-013-9823-0

Skamarock, W. C., Klemp, J. B., Dudhia, J., Gill, D. O., Barker, D. M., Duda, M. G., et al. (2008), A description of the Advanced Research WRF version 3. NCAR Technical Note TN-475+STR, NCAR, Boulder

Smagorinsky, J. (1963). General circulation experiments with the primitive equations, Part I: the basic experiment. *Monthly Weather Review*, *91*(3), 99–164. https://doi.org/10.1175/1520-0493(1963)091<0099:GCEWTP>2.3.CO;2

Sorbjan, Z. (1986). On similarity in the atmospheric boundary layer. *Boundary-Layer Meteorology*, *34*(4), 377–397. https://doi.org/10.1007/BF00120989

Stull, R. B. (1988). *An introduction to boundary layer meteorology*. Springer Netherlands. https://doi.org/10.1007/978-94-009-3027-8

Sullivan, P. P., McWilliams, J. C., & Moeng, C.-H. (1994). A subgrid-scale model for large-eddy simulation of planetary boundary-layer flows. *Boundary-Layer Meteorology*, *71*(3), 247–276. https://doi.org/10.1007/BF00713741

Wyngaard, J. C., Peltier, L. J., & Khanna, S. (1998). LES in the surface layer: Surface fluxes, scaling, and SGS modeling. *Journal of the Atmospheric Sciences*, *55*(10), 1733–1754. https://doi.org/10.1175/1520-0469(1998)055<1733:LITSLS>2.0.CO;2

Zeng, X., Zhao, M., & Dickinson, R. E. (1998). Intercomparison of bulk aerodynamic algorithms for the computation of sea surface fluxes using TOGA COARE and TAO data. *Journal of Climate*, *11*(10), 2628–2644. https://doi.org/10.1175/1520-0442(1998)011<2628:IOBAAF>2.0.CO;2

Zhou, B., Sun, S., Sun, J., & Zhu, F. (2019). The universality of the normalized vertical velocity variance in contrast to the horizontal velocity variance in the convective boundary layer. *Journal of the Atmospheric Sciences*, *76*(5), 1437–1456. https://doi.org/10.1175/JAS-D-18-0325.1

Zhou, B., Sun, S., Yao, K., & Zhu, K. (2018). Re-examining the gradient and counter-gradient representation of the local and non-local heat fluxes in the convective boundary layer. *Journal of the Atmospheric Sciences*, *75*(7), 2317–2336. https://doi.org/10.1175/JAS-D-17-0198.1